# Cationic cholesterol-dependent LNP delivery to lung stem cells, the liver, and heart

Afsane Radmand<sup>a,b</sup>, Hyejin Kim<sup>c</sup>, Jared Beyersdorf<sup>c</sup>, Curtis N. Dobrowolski<sup>c</sup>, Ryan Zenhausern<sup>c</sup> 📵, Kalina Paunovska<sup>c</sup>, Sebastian G. Huayamares<sup>c</sup> 🗓, Xuanwen Hua<sup>c</sup>, Keyi Han<sup>c</sup> 🗓, David Loughrey<sup>c</sup>, Marine Z. C. Hatit<sup>c</sup>, Ada Del Cid<sup>c</sup>, Huanzhen Ni<sup>c</sup>, Aram Shajii<sup>c</sup>, Andrea Li<sup>c</sup>, Abinaya Muralidharan<sup>d,e</sup>, Hannah E. Peck<sup>c</sup>, Karen E. Tiegreen<sup>c</sup>, Shu Jia<sup>c</sup>, Philip J. Santangelo<sup>c</sup>, and James E. Dahlman<sup>c,1</sup>

Edited by Sangeeta Bhatia, Massachusetts Institute of Technology, Cambridge, MA; received June 26, 2023; accepted September 22, 2023

Adding a cationic helper lipid to a lipid nanoparticle (LNP) can increase lung delivery and decrease liver delivery. However, it remains unclear whether charge-dependent tropism is universal or, alternatively, whether it depends on the component that is charged. Here, we report evidence that cationic cholesterol-dependent tropism can differ from cationic helper lipid-dependent tropism. By testing how 196 LNPs delivered mRNA to 22 cell types, we found that charged cholesterols led to a different lung:liver delivery ratio than charged helper lipids. We also found that combining cationic cholesterol with a cationic helper lipid led to mRNA delivery in the heart as well as several lung cell types, including stem cell-like populations. These data highlight the utility of exploring charge-dependent LNP tropism.

mRNA | LNP | barcoding | nanoparticle | scRNA-seq

Lipid nanoparticles (LNPs) have delivered RNA therapies to hepatocytes in patients after intravenous administration (1-3). As a result, there is an interest in delivery to nonliver tissues (4), which is often accomplished using three approaches. The first is to inhibit the uptake of LNPs or the subsequent activity of the therapeutic payload in the liver (5, 6). The second is to add active targeting ligands including antibodies or small molecules onto LNPs to redirect them from hepatocytes (7–11). Finally, the third is to modify the chemical composition of the LNP, thereby driving endogenous trafficking (12) away from hepatocytes. This can be accomplished by engineering the ionizable lipid (13-15) or adding a charged helper lipid, which can increase the nonliver:liver tropism (16-20). In one example, scientists found that RNA-lipoplexes were targeted to the lung or lymphoid tissues by adding positive or negative charge, respectively (16). In another, replacing the zwitterionic phospholipid 1,2-dioleoyl-sn-glycero-3-phosphoethanolamine with the cationic helper lipid 1,2-dioleoyl-3-trimethylammonium-propane (DOTAP) redirected LNPs from the liver to the lung (17). Additional observations, including that LNPs formulated with a fifth cationic component can be redirected to the lung, were subsequently reported (18–20). Given the consistency of reports showing increased lung: liver delivery after adding a cationic helper lipid, one reasonable hypothesis is that charge-dependent tropism is universal and therefore any positively charged component should increase lung delivery while decreasing liver delivery. However, other observations suggest that LNP tropism can be complex, including data that cholesterol structure can influence delivery potentially by influencing endocytosis (21-23). Taken together, these data led us to hypothesize that charged cholesterols could influence non-liver delivery differently from charged helper lipids.

### **Results**

Downloaded from https://www.pnas.org by 107.115.159.5 on March 7, 2024 from IP address 107.115.159.5.

We tested this hypothesis by quantifying how 196 LNPs delivered mRNA in vivo to 22 cell types across five tissues (SI Appendix, Fig. S1). We performed four experiments; each experiment tested one library with a given charge. One library, which served as a negative control for lung delivery, contained LNPs with neutral cholesterol and neutral helper lipids and was therefore named (0 0). The three other libraries contained neutral cholesterol and cationic helper lipids (0 +), which have been reported to increase lung delivery and decrease liver delivery (16-20); cationic cholesterols and neutral helper lipids (+ 0); or cationic cholesterols and cationic helper lipids (+ +) (SI Appendix, Fig. S2). To ensure that any differences in delivery were driven by cholesterol or helper lipid charge, we used the validated ionizable lipid cKK-E12 (24) and the poly(ethylene glycol)-lipid (PEG-lipid) C<sub>14</sub>PEG<sub>2000</sub> in all four libraries. To control for molar ratio-dependent effects, we formulated each LNP using eight ratios (SI Appendix, Fig. S3A). This resulted in 216 chemically distinct LNPs (Fig. 1 A and B). After formulating the LNPs using a microfluidic device

# **Significance**

Adding cationic helper lipids to lipid nanoparticles (LNPs) increases lung delivery and decreases liver delivery. However, the universality of the relationship between charge and LNP targeting remains unclear. Here, we report that cationic cholesterol-dependent tropism can differ from cationic helper lipid-dependent tropism, along with the development of an LNP that delivers mRNA to the heart as well as lung stem cells. These data provide evidence that charge-dependent tropism may be useful for genetic diseases requiring delivery to multiple tissues.

Author affiliations: aPetit Institute for Bioengineering and Biosciences, Georgia Institute of Technology, Atlanta, GA 30332; <sup>b</sup>Department of Chemical Engineering, Georgia Institute of Technology, Atlanta, GA 30332; Wallace H. Coulter Department of Biomedical Engineering, Georgia Institute of Technology and Emory University School of Medicine, Atlanta, GA 30332; dGeorge W. Woodruff School of Mechanical Engineering, Georgia Institute of Technology, Atlanta, GA 30332; and <sup>e</sup>Institute for Electronics and Nanotechnology, Georgia Institute of Technology, Atlanta, GA 30332

Author contributions: A.R., H.K., K.P., X.H., S.J., and P.J.S. designed research; A.R., H.K., J.B., R.Z., S.G.H., K.H., D.L., M.Z.C.H., A.D.C., H.N., A.S., A.L., A.M., H.E.P., S.J., and P.J.S. performed research; A.R., H.K., S.J., and P.J.S. contributed new reagents/analytic tools; A.R., H.K., C.N.D., K.E.T., S.J., and P.J.S. analyzed data; and A.R., K.E.T., S.J., P.J.S., and J.E.D. wrote the paper.

Competing interest statement: J.E.D. is an advisor to GV, Nava Therapeutics, and Edge Animal Health. All other authors declare no competing interests.

This article is a PNAS Direct Submission.

Copyright © 2024 the Author(s). Published by PNAS. This open access article is distributed under Creative Commons Attribution-NonCommercial-NoDerivatives License 4.0 (CC BY-NC-ND).

<sup>1</sup>To whom correspondence may be addressed. Email: james.dahlman@emory.edu.

This article contains supporting information online at https://www.pnas.org/lookup/suppl/doi:10.1073/pnas. 2307801120/-/DCSupplemental.

Published March 4, 2024.

(25), we examined the relationship between chemical composition and hydrodynamic diameter using dynamic light scattering (DLS). We found that LNPs formulated with neutral cholesterol and cationic helper lipids formed statistically larger particles than the other groups; one caveat is that the number of particles per group was very large (Fig. 1C). We did not observe statistically significant relationships between hydrodynamic diameter and cholesterol or helper lipid molar ratios (Fig. 1 D and E). In all four libraries, over 85% of the LNPs had hydrodynamic diameters less than 200 nm as well as monodisperse DLS spectra, and the hydrodynamic diameter of the libraries was consistent after 3 wk of storage at 4 °C (SI Appendix, Fig. S3B). Finally, we imaged all four libraries using transmission electron microscopy (TEM) and again found small, stable LNPs (SI Appendix, Fig. S3C). These biophysical data led us to conclude that changing the charge of different components does not substantially change the LNP structure.

We then measured how the four libraries delivered mRNA in 22 cell types across the liver, lung, heart, kidney, and spleen, using Fast Identification of Nanoparticle Delivery (26) to assess how many distinct LNPs functionally delivered mRNA to cells at once. We formulated each LNP with Cre mRNA and a unique DNA barcode. LNP N with chemical structure N was formulated with Cre mRNA and DNA barcode N; by using sensitive barcodes (27), we were able to formulate the LNPs with an mRNA:barcode mass ratio of 10:1. We then pooled monodisperse LNPs with hydrodynamic diameters less than 200 nm into their designated libraries

and individually administered them to Ai14 mice at a total dose of 1.3 mg/kg (Fig. 2A). In these mice, cells express tdTomato if Cre mRNA is translated into functional Cre protein (17). We therefore injected mice with the barcoded LNPs, waited for tdTomato expression to occur (26), isolated tdTomato<sup>+</sup> cells using fluorescence-activated cell sorting (FACS), and sequenced barcodes within the tdTomato<sup>+</sup> cells (*SI Appendix*, Fig. S4A). We did not observe statistically significant changes in weight in LNP-treated mice compared to PBS (phosphate-buffered saline)-treated mice (*SI Appendix*, Fig. S4B). As a control, we included two unencapsulated DNA barcodes, which should not enter cells as readily as DNA barcodes contained within LNPs; as expected, the counts of these negative controls were low (Fig. 2B).

When we quantified the percentage of tdTomato<sup>+</sup> cells in all live cells isolated from the tissues, we were surprised to observe that LNPs formulated with cationic cholesterols and neutral helper lipids robustly delivered mRNA to the liver (Fig. 2C). As a control, we found that LNPs formulated with neutral cholesterol and cationic helper lipids detargeted the liver as previously reported (18–20). The difference in liver delivery was not likely driven by overall LNP potency since both libraries showed similar lung delivery (Fig. 2C). Given the unexpected liver delivery with (+0) LNPs, we compared delivery in five cell types isolated from the liver. We found a significant increase in delivery, relative to (0 +) LNPs, across all hepatic cells (Fig. 2D and SI Appendix, Fig. S5A). We performed the same analysis in the lung and found that

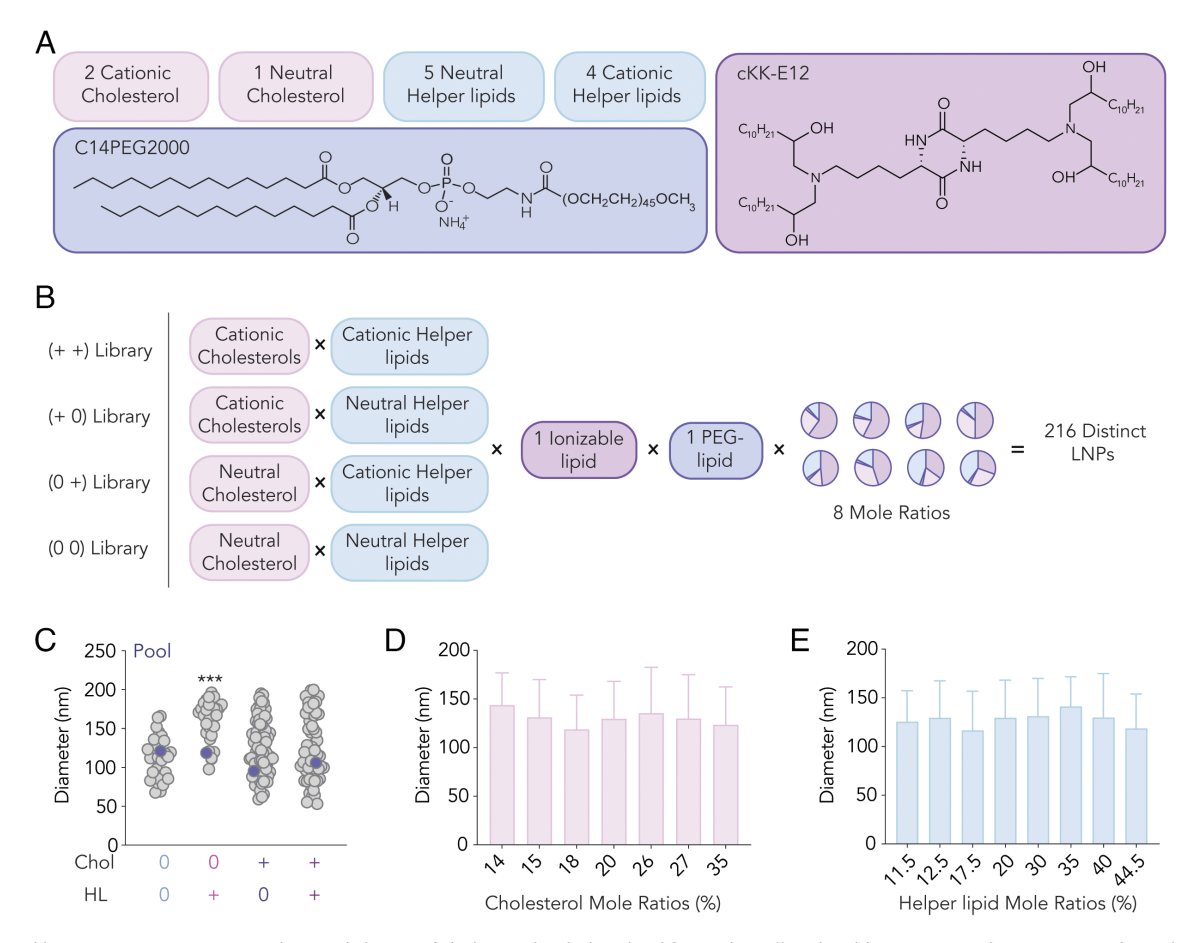
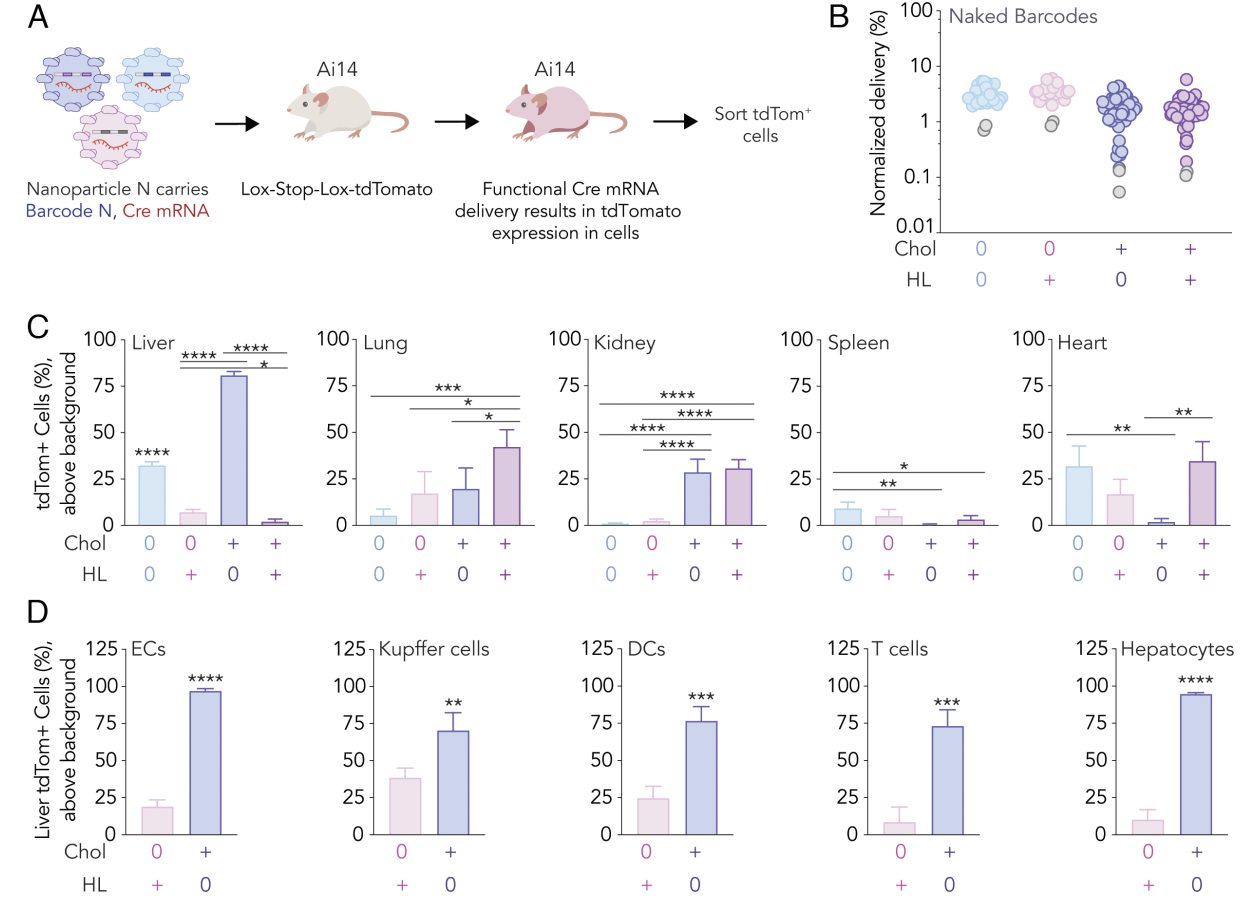


**Fig. 1.** Four libraries containing LNPs with varied charge of cholesterol or helper lipid formed small and stable LNPs. (A and B) LNPs were formulated at eight different mole ratios of the four components by varying nine helper lipids and three cholesterols, creating 216 LNPs in total. (C) LNPs in each library (gray) formed small (50 to 200 nm) LNPs with the pool diameter (purple) being in the range of the pooled LNPs from each library, indicating no LNP aggregation. The (0 +) library consisted of LNPs with significantly larger diameter. The reported diameters include all eight tested molar ratios. One-way ANOVA, mean diameter of each library was compared to the mean diameter of every other library, \*\*\*\*P < 0.0003. LNP diameter, reported from the four libraries combined, was independent of (D) cholesterol molar ratio and (E) helper lipid molar ratio, average ± SD.



although the LNPs behaved similarly when averaged across the entire tissue (Fig. 2C), there were cell type–dependent differences within the lung (*SI Appendix*, Fig. S5B). Additionally, a differential mRNA delivery to cell types across kidney, spleen, and heart was observed (*SI Appendix*, Fig. S5 *C–E*). These data are consistent with the hypothesis that LNPs containing cationic cholesterols can behave differently from LNPs containing cationic helper lipids.

One limitation to these results is that they were generated by a pool of LNPs. We therefore evaluated the hypothesis using individual LNPs. We formulated an LNP, named LNP<sup>0+</sup> for simplicity, with 57.5% cKK-E12, 2.5% C<sub>14</sub>PEG<sub>2000</sub>, 20% neutral cholesterol, and 20% cationic helper lipid. The second LNP, named LNP<sup>+0</sup>, had the same molar percentages of cKK-E12 and C<sub>14</sub>PEG<sub>2000</sub>, 20% cationic cholesterol, and 20% neutral helper lipid (Fig. 3 *A* and *B*). These two LNPs swap the cationic component while keeping an identical molar percentage of the positive charge. We chose the specific helper lipids and cholesterols for the LNPs based on structure–function analysis from the screening experiment (*SI Appendix*, Figs. S6 and S7). We formulated these LNPs to carry Cre mRNA and intravenously injected them into Ai14 mice at a dose of 1.0 mg/kg, then quantified tdTomato expression in cell types from the liver, lung, heart, kidney, and

spleen. In all liver cell types, we observed a significant increase in  $tdTomato^+$  cells from mice treated with  $LNP^{+0}$  compared to cells from mice treated with  $LNP^{0+}$  (Fig. 3C). Once again, increased liver delivery mediated by  $LNP^{+0}$  was not likely due to increased delivery in all organs (Fig. 3D–G). These data provided additional evidence that the nonliver:liver tropism of LNPs with cationic cholesterols can differ from LNPs with cationic helper lipids.

The screening data (Fig. 2C) also led us to hypothesize that formulating an LNP with cationic cholesterol and cationic helper lipid could affect nonliver:liver tropism. We therefore selected a lead LNP from the (+ +) library. Specifically, we performed enrichment analysis (14, 20, 28, 29), which can identify relationships between LNP structure and DNA barcode delivery (SI Appendix, Fig. S8A). Based on this analysis, we chose an LNP formulated with DC-cholesterol and DOTAP as it had the highest normalized delivery and was consistently positively enriched across all the cell types (Fig. 4A and SI Appendix, Fig. S8 B-E), which we named LNP++. We characterized LNP++ after formulating it with Cre mRNA (SI Appendix, Fig. S9), intravenously injected it into Ai14 mice at a dose of 1.0 mg/kg, and then quantified tdTomato expression in five organs (Fig. 4 B and C and SI Appendix, Fig. S10). In addition to high lung delivery, we found that nearly 50% of the endothelial cells (ECs) in the heart expressed tdTomato. Since we

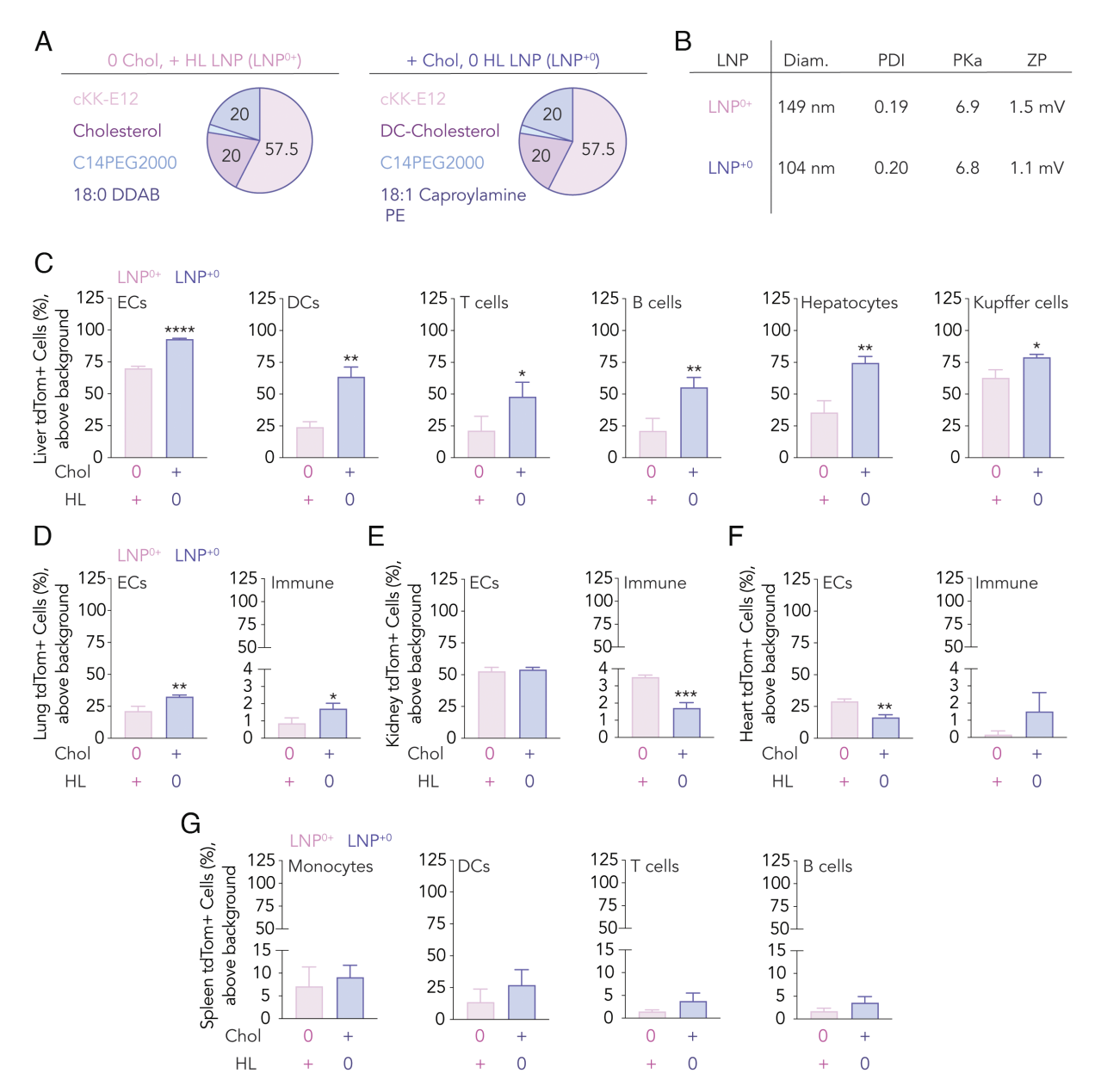


**Fig. 3.** Location of positive charge impacts systemic in vivo nonliver:liver mRNA delivery. (*A*) Top-performing LNPs from (0 +) and (+ 0) screens carrying the same mole ratios of four components. (*B*) These LNPs formed small and monodisperse particles and carried similar positive charge. (*C*) LNP<sup>+0</sup> outcompetes LNP<sup>0+</sup> in liver delivery in all cell types. mRNA delivery was also quantified in (*D*) lung, (*E*) kidney, (*F*) heart, and (*G*) spleen. (*D*–*F*) LNP<sup>+0</sup> and LNP<sup>0+</sup> led to a significant differential mRNA delivery to lung ECs, lung immune cells, kidney immune cells, and heart ECs. Unpaired *t* test, \*\*\*\*P < 0.0001, \*\*\*P = 0.0009, \*\*P < 0.0095, \*P < 0.045, average ± SD.

do not normally observe robust cardiovascular endothelial delivery, we confirmed it using several techniques. We first used high-resolution Fourier light-field microscopy (HR-FLFM) volumetric imaging (30) (Fig. 4D and SI Appendix, Fig. S11), which generated an image of cells as they passed through a flow cytometry machine. These images confirmed tdTomato expression in heart ECs. We then performed RNAscope in situ hybridization imaging (31) and again observed delivery (Fig. 4E and SI Appendix, Fig. S12). Using all three techniques (flow cytometry, flow imaging, and RNAscope), we also observed more lung mRNA delivery than liver delivery.

Finally, to understand the cell subtypes targeted by LNP<sup>++</sup> in the heart and lung, we used the single-cell RNA sequencing (scRNA-seq) approach to quantify LNP delivery in transcriptionally defined cells (20, 32, 33). After injecting mice with PBS or

LNP\*\* carrying Cre mRNA at 1.0 mg/kg, we waited 3 d, isolated the lung and heart, and quantified tdTomato mRNA, which is only transcribed if Cre mRNA has turned into functional Cre protein that leads to tdTomato mRNA transcription. We processed the data using Seurat (34) and analyzed it with BBrowser from BioTuring (35). In the heart, we observed higher delivery in capillary arterial ECs (PECAM1\*, CXCL12\*, Rbp7\*, Mgll\*, Ly6c1\*, and Aqp7\*), arterial ECs (Fbln5\*, Hey1\*, and Mecom\*), endocardial ECs (NPR3\*, Cdh11\*), capillary ECs (Rgcc\*), and lymphatic ECs (CCL21a\*, Prox1\*, and Lyve1\*). We noted evidence of delivery in dendritic cells (CD209a\*, Ifi30\*, CD209d\*, Tnfsf9\*, CD74\*, and Irf8\*) and MHC II\* resident macrophages (C1qa\*, C1qb\*, C1qc\*, and Pf4\*) (Fig. 4 F and G and SI Appendix, Fig. S13), providing very early evidence that LNPs may also reach and transfect nonendothelial cell types in the heart. The identified

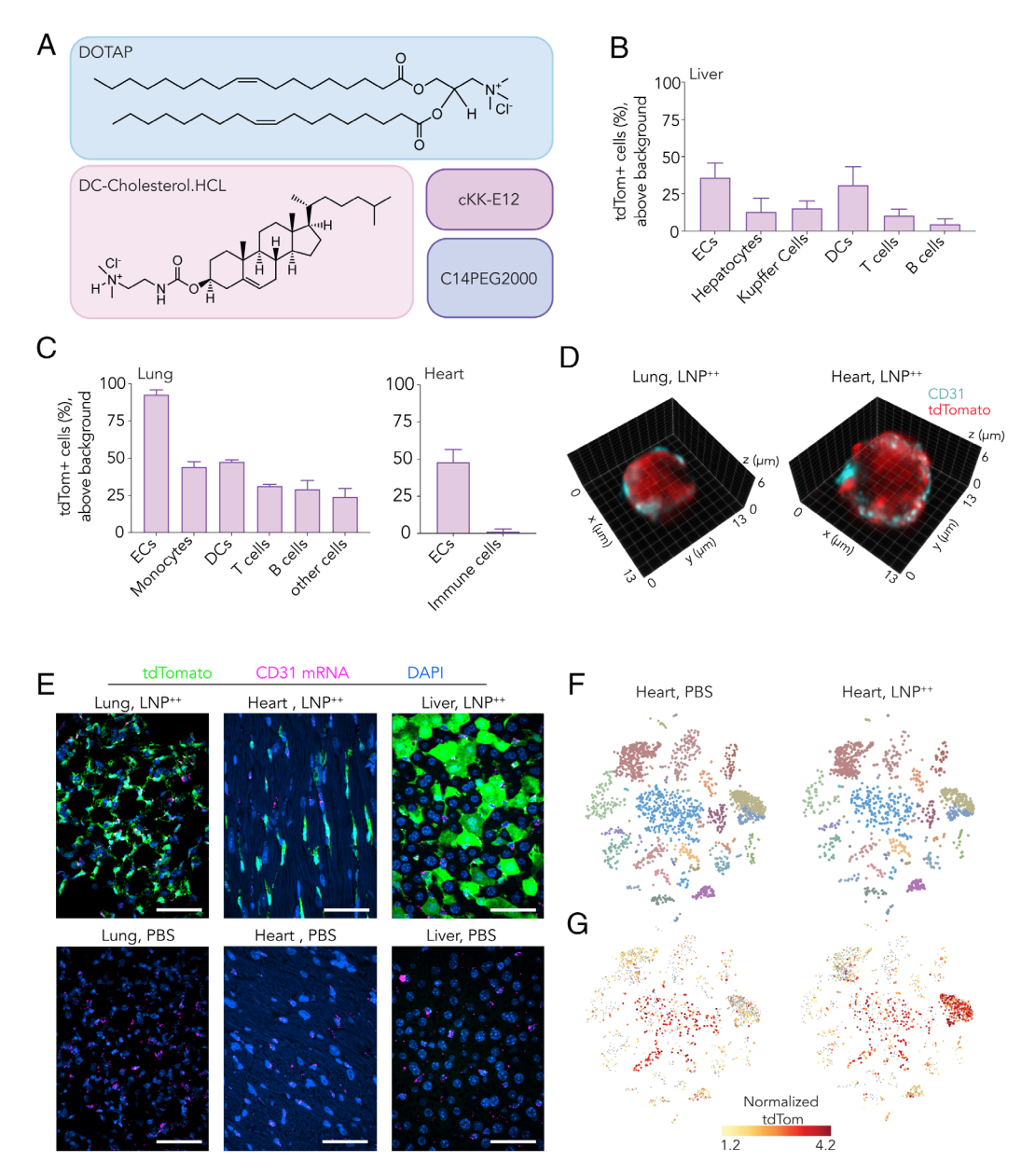


**Fig. 4.** LNP<sup>++</sup> delivers mRNA to heart ECs as well as lung cell types. (*A*) LNP<sup>++</sup> was composed of DC-cholesterol and DOTAP as cationic cholesterol and cationic helper lipid components, respectively. (*B* and *C*) LNP<sup>++</sup> improved lung:liver mRNA delivery and led to significant heart EC delivery. Average ± SD. (*D*) LNP<sup>++</sup> targeted lung and heart imaged at single-cell level using HR-FLFM. (*E*) RNAscope imaging of lung, heart, and liver. Scale bar on the image: 50 μm. (*F*) t-SNE plot representation of heart cells isolated from mice injected with either PBS or LNP<sup>++</sup>. (*G*) tdTomato mRNA expression was overlaid on heart cells. LNP<sup>++</sup> predominantly delivered mRNA to heart ECs confirmed at single-cell level via scRNA-seq.

cell populations were consistent with previously reported populations (36–38). In the lung, LNP<sup>++</sup> delivered to cell types more broadly, including VCAM1<sup>+</sup> ECs (Vwf<sup>+</sup>, Tmem100<sup>+</sup>, and Plac8<sup>+</sup>), capillary ECs (Ednrb<sup>+</sup>, Tmem100<sup>+</sup>, and Vwf<sup>-</sup>), and vascular ECs (Tmem100<sup>+</sup>, Vwf<sup>-</sup>, and Ednrb<sup>-</sup>). Again, we observed delivery in nonendothelial cell types including smooth muscle cells (Col1a2<sup>+</sup> and Acta2<sup>+</sup>), myofibroblasts (Col1a2<sup>+</sup>, Wif1<sup>+</sup>, Fgf18<sup>+</sup>, and Aspn<sup>+</sup>), fibroblasts (Col1a2<sup>+</sup>), interstitial fibroblasts (Col1a2<sup>+</sup>, Dcn<sup>+</sup>, and Inmt<sup>+</sup>), immune cells (Ptprc<sup>+</sup>), megakaryocytes (Ppbp<sup>+</sup>), type 1 pneumocytes (Rtkn2<sup>+</sup>), ciliated cells (Epcam<sup>+</sup> and Foxj1<sup>+</sup>), club cells (Epcam<sup>+</sup>, Scgb1a1<sup>+</sup>, and Sftpd<sup>+</sup>), and goblet cells (Epcam<sup>+</sup> and Bpifb1<sup>+</sup>) (SI Appendix, Fig. S14).

After making the observation that LNP<sup>++</sup> delivered mRNA to several cell populations in the lung, we confirmed delivery to these cells using flow cytometry. Specifically, we added additional flow

cytometry markers into our panel to quantify delivery in lung epithelial cells, alveolar epithelial cells, bronchial epithelial cells, and bronchioalveolar stem cells (Fig. 5 *A* and *B*). Given that our delivery studies had been performed with Cre mRNA, we also changed the mRNA payload, formulating LNP<sup>++</sup> with mRNA encoding anchored VHH (aVHH), a species-agnostic reporter (39) that does not require a transgenic Ai14 mouse (40). One day after injecting wild-type mice with 1.5 mg/kg aVHH mRNA, we quantified aVHH protein across five organs. Consistent with our previous readouts, LNP<sup>++</sup> delivered mRNA more robustly to the lung and heart compared to the liver (Fig. 5*C* and *SI Appendix*, Fig. S15), and once again we observed delivery to lung epithelial cells as well as stem-like cells (Fig. 5*C*). LNP<sup>++</sup> formulated with aVHH or Cre mRNA did not lead to significant weight changes relative to PBS-treated mice (*SI Appendix*, Fig. S16). We observed

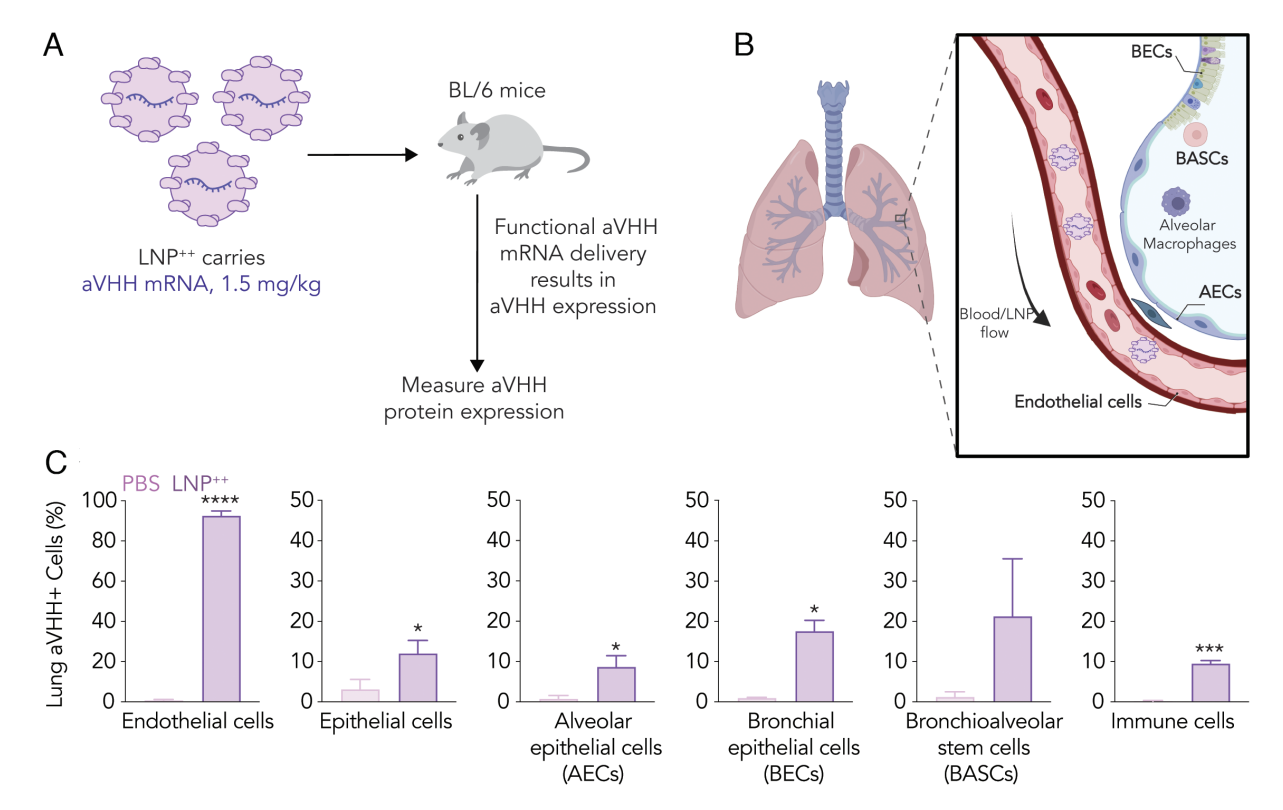


**Fig. 5.** LNP<sup>++</sup> mediates systemic lung epithelial and stem-like cell mRNA delivery. (*A*) LNP<sup>++</sup> carrying aVHH mRNA was injected to BL/6 mice at a dose of 1.5 mg/kg. One day postinjection, aVHH expression was measured in lung, heart, kidney, liver, and spleen. (*B*) mRNA delivery to lung non-EC cell types, which are less physically accessible through blood vessels, was explored. (*C*) LNP<sup>++</sup> led to mRNA delivery to epithelial cells, stem-like cells, and immune cells. Unpaired *t* test, \*\*\*\*P < 0.0001, \*\*\*P = 0.0005, \*P < 0.048, average ± SD.

some increases in cytokines relative to PBS-treated mice at 6 h (*SI Appendix*, Fig. S17), which is consistent with other LNPs that lead to transient activation of cytokines (41).

## **Discussion**

LNPs formulated with charged helper lipids regularly increase lung delivery and decrease liver delivery, suggesting that charge may be a driving factor in tropism. Here, we report evidence that cationicdependent tropism may depend on the component that is charged. While our data imply that cationic cholesterols should be considered in future LNP formulations, there were also several limitations to the study. First, our findings are in mice; anatomical, physiological, or genetic differences may make delivery different in nonhuman primates (42). Second, we have yet to investigate the underlying biological mechanism (43) behind the changes in tropism observed with LNP<sup>+0</sup> relative to LNP<sup>0+</sup>. Three mechanisms we plan to explore are serum protein adsorption, interactions with endocytosis receptors, and postendocytosis translational processing by the cell. Third, while we made observations using many LNPs, all of them were formulated with cKK-E12. It will therefore be important to understand if this observation is made with many other ionizable lipids. Finally, LNP++ led to some elevated cytokines at early timepoints in mice. It will therefore be necessary to characterize the therapeutic window of the LNP in small animals and determine whether this is sufficient for studies in larger species.

Despite these limitations, we believe these data highlight a few lessons. First, it is possible that charge-dependent delivery can reach a combination of nonliver tissues as well as liver. We envision future studies that will fine-tune delivery across several tissues. Notably, in addition to the cationic cholesterol-mediated liver, lung, and heart mRNA delivery, our study also suggests early evidence of

cationic cholesterol-dependent mRNA delivery to the kidney, which supports further exploration for refining charge-mediated systemic mRNA delivery to this organ. Second is the utility of quantifying delivery in many cell types instead of whole organs. By using scRNA-seq-based assays to read out delivery in transcriptionally defined cells, we found early evidence suggesting that LNPs may reach nonendothelial cell types in the heart. It would have been very difficult to quantify delivery to all the cell subtypes using a more traditional method. Now that we can measure delivery into these cell types, it is possible to optimize delivery in them. These data also suggest that lung epithelial and stem-like populations can be transfected via intravenous administration, which may be useful for several genetic disorders with lung phenotypes. Finally, the data generated with LNP<sup>+0</sup> point to the ability to target lung and liver at the same time, which could be useful for genetic diseases with phenotypes in both tissues, such as alpha-1 antitrypsin deficiency (44). Taken together, these lessons provide a rationale for continued work on fine-tuning charge-mediated LNP delivery.

#### **Materials and Methods**

**mRNA Synthesis.** mRNA was synthesized as previously described (20, 39, 40, 45). The mRNA sequence was made from a gBlock of DNA purchased from Integrated DNA Technologies. The 5' UTR contained a Kozak sequence, whereas the 3' UTR was designed with sequences from murine alpha-globin. In vitro transcription was performed overnight at 37 °C.

**LNP Formulation.** LNPs were created by mixing fluids together in a microfluidic device (25, 46). In the 100% ethanol phase, we added all the lipid components. In the low pH 10 mM citrate phase, we added the nucleic acids. The PEG-lipid, helper lipid, and cholesterol were purchased from Avanti.

Nanoparticle Characterization. LNP hydrodynamic diameter and polydispersity index were measured using DLS (DynaPro Plate Reader II, Wyatt). Monodisperse LNPs with 50 nm < hydrodynamic diameter < 200 nm were pooled and dialyzed into 1X PBS. Next, the mRNA concentration was measured using NanoDrop (Thermo Fisher Scientific) following sterile purification using a 0.22-µm filter (Foxx Life Sciences). Prior to injection, a portion of the LNP pool ("input") was kept for the normalization step of next-generation sequencing (NGS) of the barcodes derived from sorted samples. The mRNA dose was adjusted by the volume of injected LNPs per gram of mice through tail vein.

As previously described(20), the Quant-iT RiboGreen RNA Assay Kit (Thermo Fisher Scientific) and the Precision Nanosystems RiboGreen assay protocol were used to quantify the encapsulation efficiency of each LNP. Fifty microliters of LNP at 0.006  $\mu$ g/ $\mu$ L was added to 50  $\mu$ L of 1XTE or 50 of 1:50 dilution of Triton X-100 (Sigma Aldrich). Following a 10-min, 37 °C incubation, 100 µL of RiboGreen reagent was added to each well, and the fluorescence (485 nm excitation, 528 nm emission) was quantified. The Zeta Potential of LNP++ and libraries were quantified using a Malvern Zetasizer Nano Z as described previously (20). A total volume of 800  $\mu$ L of the particles was loaded into a Malvern disposable folded capillary cell. The settings were established as 1.4 (material refractive index), 0.01 (absorbance), 0.79 (dielectric), and 0.882 (cp).

The pKa of LNP  $^{++}$  was determined following the previously described method (20, 46). A solution containing 10 mM HEPES, 10 mM MES, 140 mM NaCl, and 10 mM NaOAc was created. The pH of the solution was decreased using HCl or increased using NaOH. One hundred forty microliters of the buffer, 5 µL of 2-(p-to luidino)-naphthalene-6-sulfonic acid, and 5  $\mu$ L of the LNP were added into a well.

**TEM Imaging.** Ten microliters of LNPs in an aqueous solution were dropped onto a carbon film-supported copper grid (Electron Microscopy Science, PA, US) for 10 min. The LNP samples were negatively stained with a 2% uranyl acetate solution for 1 min after being loaded onto the grid. The size and morphology of the samples were then captured using a 120 kV TEM.

Animal Experiments. All mouse experiments were performed with approval from the Georgia Tech IACUC. Ai14 mice were bred at Georgia Tech, whereas BL/6 mice were purchased (Jackson Labs). N = 2 to 4 mice/group were used unless otherwise noted.

Cell Isolation and Staining. The lung, liver, spleen, kidney, and heart were extracted after mice were perfused with 1X PBS via the right atrium. For the heart, we used collagenase IV (10 mg/mL) as a digestive enzyme. For the spleen, no digestive enzymes were needed. The other tissues used collagenase type I, collagenase XI, and hyaluronidase. For the heart, we used collagenase IV. The cell suspensions were filtered through a 70-µm sterile nylon mesh cell strainer, washed with 1X PBS, and transferred to Eppendorf tubes. Fc receptors were blocked using TruStain fcX™ anti-mouse CD16/32 (BioLegend). The following antibodies were used: clone 6D5, 17A2, N418, M1/70, FA11, 30-F11, and 390. We also used anti-TER-119 (TER-119, BioLegend), anti-Annexin V (BioLegend), DAPI for nucleic acid staining (Sigma-Aldrich), PE anti-mCD47 (miap301, BioLegend), CD326 (G8.8, BioLegend), anti-Sca-1 (D7, BioLegend), anti-CD24 (M1/69, BD Biosciences), anti-CD271 (ME20.4, Invitrogen), and Monorab™ Rabbit Anti-Camelid VHH antibody, mAb (96A3F5, GenScript). Each stain was added at a 1:200 dilution to the cell suspension. Flow gating is shown (SI Appendix, Figs. S18 and S19). When Ai14 mice were used to quantify delivery, we also used PBS-treated Ai14 mice to control for flow gating.

PCR Amplification. We amplified samples using previously described methods

Data Normalization. Count of each barcode was normalized to the total count per sorted sample. Then it was normalized to the count of each barcode in input (the pool of LNP injected into mice) (26).

Data Analysis and Statistics. We processed sequencing results using a Python-based tool. These counts were then subsequently analyzed using R before GraphPad Prism was used to plot the data. Data are plotted as mean and SD.

Cytokine Analysis. As described previously (20), 6 h after intravenous administration of LNP<sup>++</sup>, lipopolysaccharide, or PBS to C57BL/6J mice, blood was collected. Serum was isolated and pooled (N = 3) before cytokine levels were measured using the Mouse Cytokine Profiler Array Panel A (R&D Systems). The images were captured using a LI-COR Odyssey CLx Far Infrared Imager, and relative concentrations were determined using ImageJ.

In Situ Hybridization and Immunostaining. mRNA transcripts were visualized using the RNAscope Multiplex Fluorescent Reagent Kit v2. After completing the RNAscope protocol, immunostaining was performed to visualize the expressed tdTomato protein. Slides were blocked and stained overnight using a goat anti-tdTomato antibody (MyBioSource MBS448092) at a 1:100 dilution, then incubated with a donkey anti-goat antibody (Thermo Fisher Scientific A-21447) at a 1:250 dilution and counterstained with DAPI.

Microscopy and Image Quantification. We acquired images using a 1.3 NA oil objective at 40x. We used a confocal microscope that included a Hamamatsu Flash 4.0v2 CMOS camera. Images were captured and preprocessed using Volocity software (PerkinElmer), and the quantification of tdTomato<sup>+</sup> cells was performed with Imaris software. Hepatocyte nuclei were segmented based on DAPI signal and volume to exclude nonparenchymal cells; nuclei were then classified based on the mean intensity of the tdTomato signal into positive and negative. In heart and lung images, single nuclei were segmented based on DAPI signal and volume to exclude cell clusters. Single nuclei were then identified as CD31<sup>+</sup> based on the mean intensity of CD31 signal, followed by subclassification into tdTomato positive and negative. The average number of tdTomato<sup>+</sup> cells was calculated across five fields of view per slide to generate biological replicates.

Single-Cell Library Preparation. Whole transcriptome analyses were conducted on whole lung and heart cells using the BD Rhapsody Single-Cell Analysis System (BD Biosciences). Dead cells and red blood cells were depleted using EasySep™ dead cell (Annexin V) and RBC (anti-TER119) removal. Each sample was incubated with unique antimouse hashtag antibodies and washed with RoboSep buffer before proceeding. For the pooled sample, a BD Rhapsody cartridge was loaded with 40,000 cells. Barcoded beads were then loaded and cells were lysed. From the mRNA and sample tags captured on beads, cDNA libraries were prepared using the BD Rhapsody Whole Transcriptome Analysis (WTA) Amplification Kit following the BD Rhapsody System mRNA WTA and Sample Tag Library Preparation protocol (BD Biosciences). The final libraries were quantified using a Qubit Fluorometer, and the size distribution was measured using Experion™ automated electrophoresis system (Bio-Rad).

The data were processed using zUMIs for the RNA mapping and counting and Salmon Alevin for the cell hashes (47, 48). All samples were mapped to GRCm39; exonic regions were counted. The output files were loaded into Seurat. Cells were log normalized to a scale factor of 10,000, then scaled using a linear transformation (34). DoubletFinder (49) was used to identify doublets. Following this, PCA and t-SNE analyses were performed and the results were exported for analysis in BBrowser2. The cell search tool was used to identify the cell types within each cluster, and tdTomato expression was overlaid on the clusters.

**HR-FLFM.** We conducted image acquisition based on a light-field imaging flow cytometer. The setup is composed of a HR-FLFM (30, 50), a microfluidics-based sample delivery system, and a stroboscopic multicolor laser illumination system. We constructed the HR-FLFM on an Eclipse Ti2-U microscope with a Plan Apo Lambda 100x 1.45 NA Oil objective (Nikon). A customized microlens array (RPC Photonics) was used to partition the light field in the Fourier domain. The HR-FLFM images were captured by an ORCA-Flash 4.0 V3 Digital CMOS camera (Hamamatsu Photonics). Samples were delivered through a microfluidic chip (Darwin Microfluidics) by a three-channel microfluidic flow controller and sensor system (Elveflow). We applied the stroboscopic illumination schemes to reduce motion blur and acquired images with a 200 Hz frame rate. The camera exposure time was set as 5 ms, while the effective exposure time with stroboscopic illumination is 100 µs.

The acquired images were filtered with a threshold to remove blank frames that had no imaging targets in the field of view. For multicolor imaging, the adjacent frames were selected and sorted into separate groups based on the fluorescence signals of subcellular structures. The sorted images then underwent rolling-ball background subtraction (51) and ACsN denoising algorithms (52) to improve the image signal-to-noise ratio. After that, we applied a circular mask to highlight each elemental image before conducting 3D reconstructions. During the reconstruction, we used a Titan RTX graphics card (Nvidia) to accelerate the Richardson-Lucy deconvolution process. We used approximately 50 iterations to achieve high-resolution subcellular imaging in each 3D volume.

Data, Materials, and Software Availability. All study data are included in the article and/or SI Appendix.

- D. Adams et al., Patisiran, an RNAi therapeutic, for hereditary transthyretin amyloidosis, N. Engl. J. Med. 379, 11-21 (2018)
- J. D. Gillmore et al., CRISPR-Cas9 in vivo gene editing for transthyretin amyloidosis, N. Engl. J. Med 385, 493-502 (2021).
- Anonymous, Intellia therapeutics presents new interim data from first-in-human study of NTLA-2002 for the treatment of hereditary angioedema (HAE) at the American College of Allergy, Asthma & Immunology 2022 Annual Scientific Meeting. https://ir.intelliatx.com/news-releases/ news-release-details/intellia-therapeutics-presents-new-interim-data-first-human (2022). Accessed 8 June 2023.
- D. Loughrey, J. E. Dahlman, Non-liver mRNA delivery. Accounts Chem. Res. 55, 13-23 (2022).
- N. R. M. Saunders et al., A nanoprimer to improve the systemic delivery of siRNA and mRNA. Nano Lett. 20, 4264-4269 (2020).
- C. D. Sago et al., Augmented lipid-nanoparticle-mediated in vivo genome editing in the lungs and spleen by disrupting Cas9 activity in the liver. Nat. Biomed. Eng. 6, 157-167 (2022).
- N. Dammes et al., Conformation-sensitive targeting of lipid nanoparticles for RNA therapeutics. Nat. Nanotechnol. 16, 1030-1038 (2021).
- R. Kedmi et al., A modular platform for targeted RNAi therapeutics. Nat. Nanotechnol. 13, 214–219 8
- N. Veiga et al., Cell specific delivery of modified mRNA expressing therapeutic proteins to leukocytes. Nat. Commun. 9, 4493 (2018).
- J. G. Rurik et al., CART cells produced in vivo to treat cardiac injury. Science 375, 91-96 (2022). 10
- D. Tarab-Ravski et al., Delivery of therapeutic RNA to the bone marrow in multiple myeloma using CD38-targeted lipid nanoparticles. Adv. Sci. 10, e2301377 (2023).
- A. Akinc et al., Targeted delivery of RNAi therapeutics with endogenous and exogenous ligand-based mechanisms. Mol. Ther. 18, 1357-1364 (2010).
- M. Qiu et al., Lung-selective mRNA delivery of synthetic lipid nanoparticles for the treatment of pulmonary lymphangioleiomyomatosis. Proc. Natl. Acad. Sci. U.S.A. 119, e2116271119 (2022).
- H. Ni et al., Piperazine-derived lipid nanoparticles deliver mRNA to immune cells in vivo. Nat. Commun. 13, 4766 (2022).
- M. P. Lokugamage, C. D. Sago, Z. Gan, B. R. Krupczak, J. E. Dahlman, Constrained nanoparticles deliver 15.
- siRNA and sgRNA to T cells in vivo without targeting ligands. *Adv. Mater.* **31**, 1902251 (2019).

  L. M. Kranz *et al.*, Systemic RNA delivery to dendritic cells exploits antiviral defence for cancer immunotherapy. Nature 534, 396-401 (2016).
- K. J. Kauffman et al., Rapid, single-cell analysis and discovery of vectored mRNA transfection in vivo with a loxP-flanked tdTomato reporter mouse. Mol. Ther. Nucleic Acids 10, 55-63 (2018).
- Q. Cheng et al., Selective organ targeting (SORT) nanoparticles for tissue-specific mRNA delivery and CRISPR-Cas gene editing. Nat. Nanotechnol. 15, 313-320 (2020).
- S. T. LoPresti, M. L. Arral, N. Chaudhary, K. A. Whitehead, The replacement of helper lipids with charged alternatives in lipid nanoparticles facilities targeted mRNA delivery to the spleen and lungs. J. Control. Release 345, 819-831 (2022), 10.1016/j.jconrel.2022.03.046.
- A. Radmand et al., The transcriptional response to lung-targeting lipid nanoparticles in vivo. Nano Lett. 23, 993-1002 (2023).
- 21. M. Herrera, J. Kim, Y. Eygeris, A. Jozic, G. Sahay, Illuminating endosomal escape of polymorphic lipid nanoparticles that boost mRNA delivery. Biomater. Sci. 9, 4289-4300 (2021).
- S. Patel et al., Boosting intracellular delivery of lipid nanoparticle-encapsulated mRNA. Nano Lett. **17**, 5711-5718 (2017).
- K. Paunovska et al., Nanoparticles containing oxidized cholesterol deliver mRNA to the liver microenvironment at clinically relevant doses. Adv. Mater. 31, e1807748 (2019), 10.1002/
- Y. Dong et al., Lipopeptide nanoparticles for potent and selective siRNA delivery in rodents and nonhuman primates. Proc. Natl. Acad. Sci. U.S.A. 111, 3955-3960 (2014).
- D. Chen et al., Rapid discovery of potent siRNA-containing lipid nanoparticles enabled by controlled microfluidic formulation. J. Am. Chem. Soc. 134, 6948-6951 (2012).
- C. D. Sago et al., High-throughput in vivo screen of functional mRNA delivery identifies nanoparticles for endothelial cell gene editing. Proc. Natl. Acad. Sci. U.S.A. 115, E9944-E9952 (2018).

ACKNOWLEDGMENTS. The work was funded by the NIH (UG3-TR002855) awarded to J.E.D. and P.J.S.), Defense Advanced Research Projects Agency (DARPA) (PREPARE grant number HR00111920008, awarded to P.J.S. and J.E.D.), NIH R35GM124846 (to S.J.), and NSF DBI2145235 (to S.J.). Fig. 5B was created using BioRender.com.

- 27. C. D. Sago et al., Modifying a commonly expressed endocytic receptor retargets nanoparticles in vivo. Nano Lett. 18, 7590-7600 (2018).
- S. G. Huayamares et al., High-throughput screens identify a lipid nanoparticle that preferentially delivers mRNA to human tumors in vivo. J. Control. Release 357, 394-403 (2023).
- C. D. Sago et al., Nanoparticles that deliver RNA to bone marrow identified by in vivo directed evolution. J. Am. Chem. Soc. 140, 17095-17105 (2018).
- X. Hua, W. Liu, S. Jia, High-resolution Fourier light-field microscopy for volumetric multi-color livecell imaging. Optica 8, 614-620 (2021).
- F. Wang et al., RNAscope: A novel in situ RNA analysis platform for formalin-fixed, paraffin-embedded tissues. J. Mol. Diagn. 14, 22-29 (2012).
- C. Dobrowolski et al., Nanoparticle single-cell multiomic readouts reveal that cell heterogeneity influences lipid nanoparticle-mediated messenger RNA delivery. Nat. Nanotechnol. 17, 871-879
- M. Z. C. Hatit et al., Nanoparticle stereochemistry-dependent endocytic processing improves in vivo mRNA delivery. Nat. Chem. 15, 508-515 (2023), 10.1038/s41557-023-01138-9
- Y. Hao et al., Integrated analysis of multimodal single-cell data. Cell 184, 3573-3587.e29 (2021)
- T. Le et al., BBrowser: Making single-cell data easily accessible. bioRxiv [Preprint] (2020). https://doi. org/10.1101/2020.12.11.414136 (Accessed 10 December 2022).
- J. Kalucka et al., Single-cell transcriptome atlas of murine endothelial cells. Cell 180, 764-779.e20 (2020).
- I. R. McCracken et al., Mapping the developing human cardiac endothelium at single-cell resolution identifies MECOM as a regulator of arteriovenous gene expression. Cardiovasc. Res. 118, 2960-2972 (2022).
- E. Martini et al., Single-cell sequencing of mouse heart immune infiltrate in pressure overload-driven heart failure reveals extent of immune activation. Circulation 140, 2089-2107 (2019).
- P. M. Tiwari et al., Engineered mRNA-expressed antibodies prevent respiratory syncytial virus infection. Nat. Commun. 9, 3999 (2018).
- M. Z. C. Hatit et al., Species-dependent in vivo mRNA delivery and cellular responses to nanoparticles. Nat. Nanotechnol. 17, 310-318 (2022).
- Anonymous, European medicines agency assessment report-Onpattro. https://www.ema.europa.eu/ en/documents/assessment-report/onpattro-epar-public-assessment-report\_.pdf (2018). Accessed
- K. Paunovska, D. Loughrey, J. E. Dahlman, Drug delivery systems for RNA therapeutics. Nat. Rev. Genet. 23, 265-280 (2022).
- A. Dilliard Sean, Q. Cheng, J. Siegwart Daniel, On the mechanism of tissue-specific mRNA delivery by selective organ targeting nanoparticles. Proc. Natl. Acad. Sci. U.S.A. 118, e2109256118 (2021).
- P. Strnad, N. G. McElvaney, D. A. Lomas, Alpha1-antitrypsin deficiency. N. Engl. J. Med. 382, 1443-1455 (2020).
- K. E. Lindsay et al., Aerosol delivery of synthetic mRNA to vaginal mucosa leads to durable expression of broadly neutralizing antibodies against HIV. Mol. Ther. 28, 805-819 (2020)
- J. E. Dahlman et al., In vivo endothelial siRNA delivery using polymeric nanoparticles with low molecular weight. Nat. Nanotechnol. 9, 648-655 (2014).
- S. Parekh, C. Ziegenhain, B. Vieth, W. Enard, I. Hellmann, zUMIs-A fast and flexible pipeline to process RNA sequencing data with UMIs. Gigascience 7, giy059 (2018).
- A. Srivastava, L. Malik, T. Smith, I. Sudbery, R. Patro, Alevin efficiently estimates accurate gene abundances from dscRNA-seq data. Genome Biol. 20, 65 (2019).
- C. S. McGinnis, L. M. Murrow, Z. J. Gartner, DoubletFinder: Doublet detection in single-cell RNA sequencing data using artificial nearest neighbors. Cell Syst. 8, 329-337.e4 (2019)
- 50 C. Guo, W. Liu, X. Hua, H. Li, S. Jia, Fourier light-field microscopy. Opt. Express 27, 25573-25594 (2019).
- S. R. Sternberg, Biomedical image processing. Computer 16, 22-34 (1983).
- B. Mandracchia et al., Fast and accurate sCMOS noise correction for fluorescence microscopy. Nat. Commun. 11, 1-12 (2020).